Flow Over a Cylinder

Gayathri Kola
The University of Texas at Arlington, Arlington, Texas, 76019, United States

In this experiment, the flow over a 2D circular cylinder in the subcritical regime is investigated using a combination of analytical methods, experimental data, and computational fluid dynamics (CFD) simulations. The study examines edge velocity distribution, drag coefficient calculation, pressure distribution, and flow separation over the cylinder. The Reynolds number for the experiment is Re_D =1.051·10^5, and comparisons are made between analytical, CFD, and experimental results. Flow separation is observed at different angles for CFD ($\theta = 80.4°$) and experimental data ($\theta = 120°$), for pressure coefficient distributions. The drag coefficient is computed through four approaches, with the CFD result significantly lower than the others, possibly due to the choice of a laminar model during the simulation and default parameter settings. The experimentally computed drag coefficient obtained is 1.16, agreeing with the literature fit. Additionally, the wall shear stress and skin friction coefficient of CFD results are analyzed to locate the flow separation point. The edge velocity profile is estimated using various methods, and a CFD simulation is rerun at a different velocity, resulting in a new separation location ($\theta = 84.00°$). The study provides insights into the complex flow behavior over a cylinder in the subcritical regime.

I. Nomenclature

ρ	=	density of air
b	=	span
c	=	chord
T	=	room temperature
R	=	gas constant of air
P	=	room pressure
L	=	lift
D	=	drag
F	=	force
ρ_∞	=	freestream density
U_∞	=	freestream velocity
P_{total}	=	total pressure
P_{static}	=	static pressure
P_{scan}	=	pressure from differential pressure scanner
P_{pitot}	=	pressure from the pitot tube
P_{local}	=	local pressure
P_∞	=	freestream pressure
C_L	=	lift coefficient
C_D	=	drag coefficient

II. Introduction

The report presents the study of flow over a two-dimensional circular cylinder in a low-speed wind tunnel at low Reynolds numbers. The surface pressure distribution, separation location at a freestream velocity, and drag forces are studied. Three different types of methods are employed: analytical methods, experimental data, and computational fluid dynamics (CFD) simulation results. The viscous flow characteristics from the experiment are compared against CFD and analytical methods.

The flow characteristics can be categorized by the Reynolds number. The Reynolds number relates the ratio of inertial forces to viscous forces. Higher values of the Reynolds number indicate higher turbulence tendencies and lower levels of viscosity. In this report, we will be examining the sub-critical regime of flow over the cylinder, however, this section presents a brief discussion of all major regimes.

Starting with low Reynolds number $Re_D < 4$, the flow is viscous in nature and the boundary layer remains attached to the surface of the cylinder. Due to dominant viscous forces, the pressure distribution is approximately symmetrical, the drag due to pressure is minimal and skin friction drag is high.

For Reynolds numbers ranging from $4 < Re_D < 40$, there is a symmetrical wake region seen on the aft part of the cylinder. This region contains a steady recirculating flow. At Reynolds number above 40, the flow in the wake region becomes unsteady and forms shedding vortices. These vortices are known as von Karman vortex sheets. The frequency of vortex shedding is represented by the Strouhal number. It is applicable for Reynolds numbers up to 10^5, an approximate constant is at 0.2. Additionally, this quantity is used to determine the time-step size calculation for setting up the CFD simulation [1].

Moving onto the subcritical, critical, and supercritical regimes; the subcritical regime begins at Reynold number higher than 400 up to 300,000 as seen in Fig 1. There is a wide wake region behind the cylinder and the laminar boundary layer separates upstream of the cylinder. This is the cause of the large turbulent wake region on the aft portion of the cylinder. Beyond this range, in between 300,000 < Re_D <1,500,000, there is a reattachment of the boundary layer causing a separation bubble. The laminar boundary layer separates and promptly undergoes transition to turbulence. The momentum gained in the turbulence energizes and attaches the boundary layer back to the surface of the cylinder. With higher energy, the wake region behind the cylinder is smaller in size. This is the critical regime [1].

Lastly, for Reynolds numbers above 1,500,000, there is turbulence seen in the forebody region of the cylinder. The higher momentum of flow delays the flow separation to the aft region. The wake region is narrow in size, similar to the critical regime except there is no separation bubble. This is known as the supercritical regime. In this experiment, the sub-critical regime is explored in detail through analytical, experimental, and numerical methods [1].

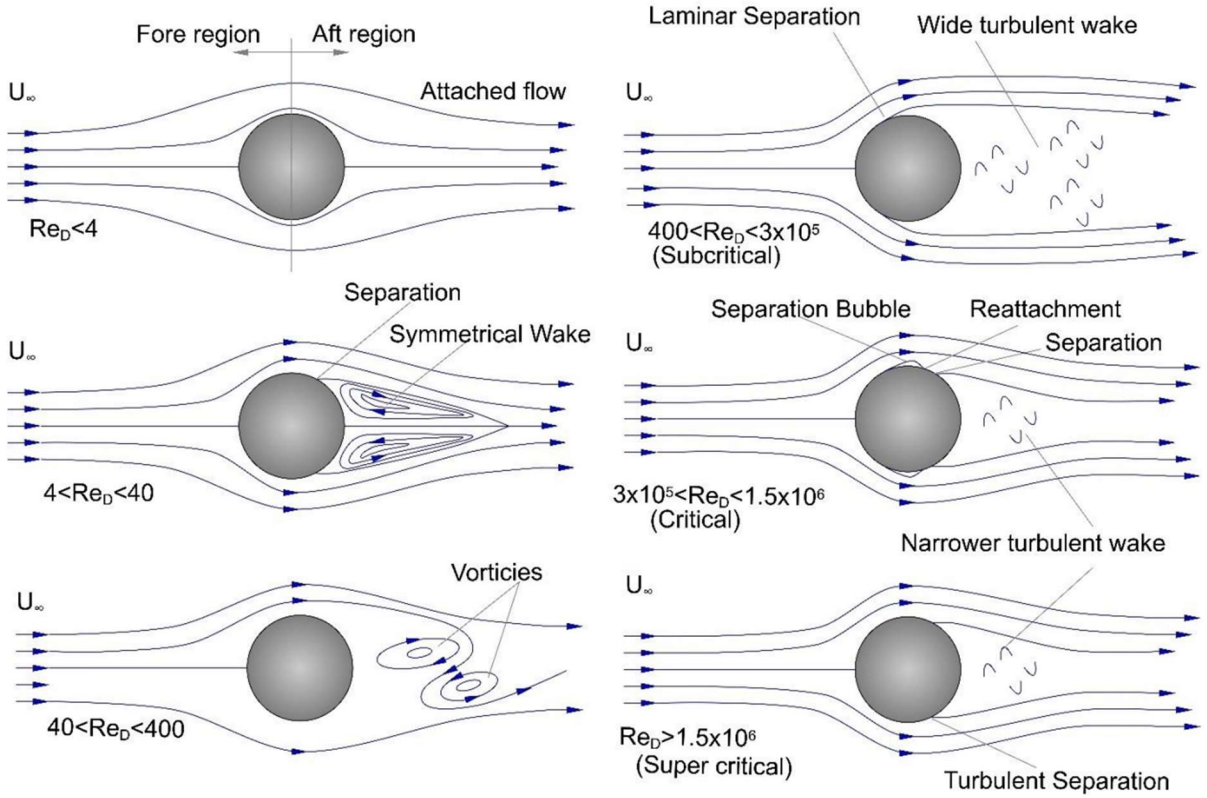

Fig. 1 Flow over a cylinder regime based on Reynolds number [1].

Three different approaches are taken to estimate the drag force, separation point, and freestream velocity – using an analytical, experimental, and computational fluid dynamics (CFD) simulation.

Three coordinate systems are used to solve problems on the cylinder–cartesian frame (x-y) located at the cylinder's axial center, polar frame (r-θ), and curvilinear frame (r-x). In this report, the angle θ is considered positive clockwise and measured from -x.

For the analytical method, the flow outside the boundary layer is assumed to be irrotational, whereas it is rotational inside. A few different analytical methods are explored in this report. With the established coordinate systems, the edge velocity distribution is made using Bernoulli's principle assuming inviscid flow over the cylinder. Potential flow theory is used with a superimposed uniform flow and doublet to mimic flow over a cylinder. For the inviscid case, the edge velocity U_e point is on the surface of the cylinder since viscous effects are neglected. Using polar coordinates, the edge velocity can be obtained by setting $r = R$ for the surface of the cylinder.

$$U_e = v_{\theta \ at \ r=R} = 2U_\infty \sin\theta \qquad\qquad v_{r \ \ at \ \ r=R} = 0 \tag{1}$$

In the case of viscous flow, a boundary layer with a displacement thickness δ develops on the surface of the cylinder. For low Mach numbers, Bernoulli's principle can be used to obtain an ideal pressure profile. This means the flow must be assumed as steady, inviscid, and incompressible flow. Two points are chosen – one at the freestream, and the second on the surface of the cylinder. A streamline connecting the two points is used to obtain the pressure coefficient for the ideal case. Using polar coordinates, Eq. (2-3) can be used to obtain the ideal surface pressure distribution in Eq.(4).

$$p_e = p_\infty + \frac{1}{2}\rho_\infty U_\infty^2 - 2\rho_\infty U_\infty^2 \sin^2\theta \tag{2}$$

$$C_p = \frac{p_e - p_\infty}{\frac{1}{2}\rho_\infty U_\infty^2} \tag{3}$$

$$C_p = 1 - 4\sin^2\theta \tag{4}$$

This ideal distribution is compared against experimental values of the pressure coefficient calculated and numerical results. The separation location for the ideal case is not present since there is no boundary layer separation. However, for the experimental and CFD cases, the separation location is much more apparent. This will be discussed in section IV.

For bluff bodies like the cylinder, there is a strong influence of downstream wake on the upstream regions. This causes a coupling between the viscous and inviscid flow which requires experimental and numerical tests to analyze the flow.

The drag coefficient and drag forces are calculated for the experimental and CFD data. For the experimental data, a corrected drag coefficient method by Allen and Vincenti is used to account for wall confinement effects for the wind tunnel. Then, the three values are compared against a curve-fit drag coefficient method by Sucker and Brauer. This is applicable for Reynolds numbers ranging from $10^{-4} < Re_D < 250{,}000$ [1].

III. Experimental Procedure

A. Apparatus

In this experiment, we utilize an AF100 low-speed wind tunnel, which is an open return suction type wind tunnel. It features a bell-mouth diffuser at the entrance that houses a honeycomb flow straightener designed to accelerate the airflow into the test section. This flow straightener effectively mitigates the lateral velocity components caused by the swirling motion of air in the room. Subsequently, the air passes through a protective grid and a variable-speed axial fan before entering the test section. The speed of the axial fan, which determines the velocity in the test section, is controlled by an electric Control and Instrumentation unit situated at the rear section of the wind tunnel. The test section itself has a transparent square cross-section with dimensions of approximately 300 mm in length. There are four ports on the top of the test section, comprising two for Pitot tubes and two for static-pressure ports. A specially designed pitot tube is affixed to the test section, capable of vertical movement up to 4 cm to access the core flow region and measure the average freestream velocity. The pitot tube is linked to a unislide (Velmex MA4039W1-S6)

controlled by a stepper controller (Velmex VXM-1), with its interface connected to a computer. The LabVIEW/ DTCNeX interface is employed for managing the control inputs [1].

Fig. 2 The AF100 Wind tunnel [1].

The cross-sectional area of the test section is $12'' \times 12''$. A custom-made Pitot tube is used to measure the average freestream velocity. It is attached to the slide, lowering to 4 cm of tunnel core from the test section wall. This measures the freestream dynamic pressure which can be observed from the manometer on the white front panel. The pressure scanner used has 32 channels of which 30 are connected to the cylinder. The primary study of importance is the region of laminar flow at the forebody. The pressure on the aft part remains constant because of flow separation. Due to this, more pressure sensors are placed on the forebody region than the aft part. The location of port positions along with the corresponding angles are given in Fig. 4. A 100 samples are collected by each scanner at the ports and an average value of the port is included in the Excel data for post-processing.

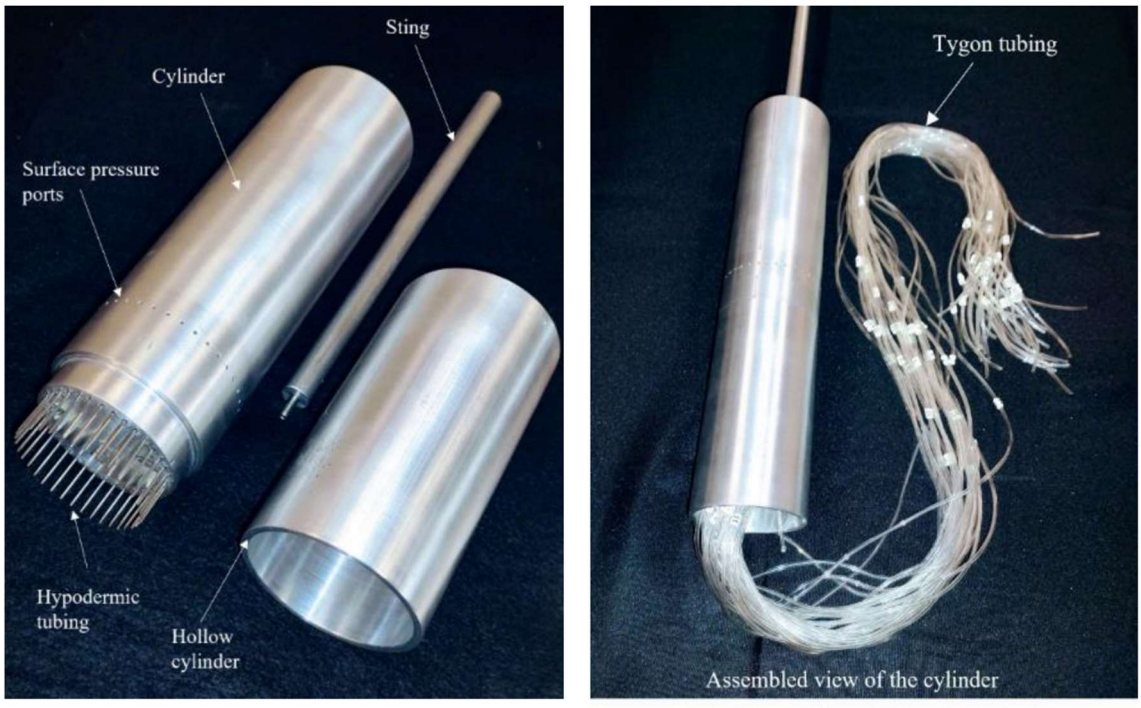

Fig. 3 Aluminium cylinder for the experiment [1].

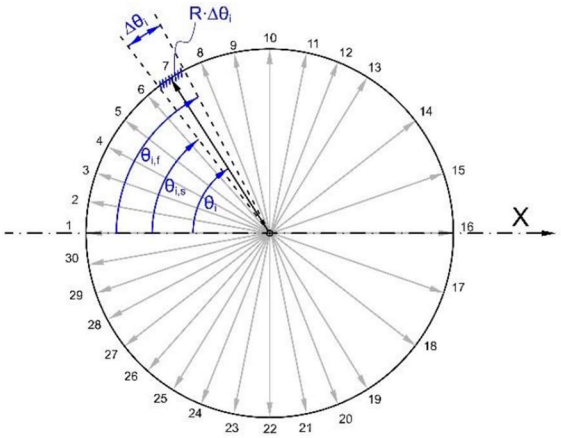

Port Name	Port Position $\theta_i[rad]$	Panel Angular Width: $\Delta\theta_i[rad]$	Panel-arc start angle $\theta_{i,s}[rad]$	Panel-arc end angle $\theta_{i,f}[rad]$
1	0	$10\cdot(\pi/180)$	$355\cdot(\pi/180)$	$5\cdot(\pi/180)$
2	$10\cdot(\pi/180)$	$10\cdot(\pi/180)$	$5\cdot(\pi/180)$	$15\cdot(\pi/180)$
3	$20\cdot(\pi/180)$	$10\cdot(\pi/180)$	$15\cdot(\pi/180)$	$25\cdot(\pi/180)$
4	$30\cdot(\pi/180)$	$10\cdot(\pi/180)$	$25\cdot(\pi/180)$	$35\cdot(\pi/180)$
5	$40\cdot(\pi/180)$	$10\cdot(\pi/180)$	$35\cdot(\pi/180)$	$45\cdot(\pi/180)$
6	$50\cdot(\pi/180)$	$10\cdot(\pi/180)$	$45\cdot(\pi/180)$	$55\cdot(\pi/180)$
7	$60\cdot(\pi/180)$	$10\cdot(\pi/180)$	$55\cdot(\pi/180)$	$65\cdot(\pi/180)$
8	$70\cdot(\pi/180)$	$10\cdot(\pi/180)$	$65\cdot(\pi/180)$	$75\cdot(\pi/180)$
9	$80\cdot(\pi/180)$	$10\cdot(\pi/180)$	$75\cdot(\pi/180)$	$85\cdot(\pi/180)$
10	$90\cdot(\pi/180)$	$10\cdot(\pi/180)$	$85\cdot(\pi/180)$	$95\cdot(\pi/180)$
11	$100\cdot(\pi/180)$	$10\cdot(\pi/180)$	$95\cdot(\pi/180)$	$105\cdot(\pi/180)$
12	$110\cdot(\pi/180)$	$10\cdot(\pi/180)$	$105\cdot(\pi/180)$	$115\cdot(\pi/180)$
13	$120\cdot(\pi/180)$	$10\cdot(\pi/180)$	$115\cdot(\pi/180)$	$125\cdot(\pi/180)$
14	$\mathbf{140\cdot(\pi/180)}$	$\mathbf{25\cdot(\pi/180)}$	$\mathbf{125\cdot(\pi/180)}$	$\mathbf{150\cdot(\pi/180)}$
15	$\mathbf{160\cdot(\pi/180)}$	$\mathbf{20\cdot(\pi/180)}$	$\mathbf{150\cdot(\pi/180)}$	$\mathbf{170\cdot(\pi/180)}$
16	$\mathbf{180\cdot(\pi/180)}$	$\mathbf{20\cdot(\pi/180)}$	$\mathbf{170\cdot(\pi/180)}$	$\mathbf{190\cdot(\pi/180)}$
17	$\mathbf{200\cdot(\pi/180)}$	$\mathbf{20\cdot(\pi/180)}$	$\mathbf{190\cdot(\pi/180)}$	$\mathbf{210\cdot(\pi/180)}$
18	$\mathbf{220\cdot(\pi/180)}$	$\mathbf{25\cdot(\pi/180)}$	$\mathbf{210\cdot(\pi/180)}$	$\mathbf{235\cdot(\pi/180)}$
19	$240\cdot(\pi/180)$	$10\cdot(\pi/180)$	$235\cdot(\pi/180)$	$245\cdot(\pi/180)$
20	$250\cdot(\pi/180)$	$10\cdot(\pi/180)$	$245\cdot(\pi/180)$	$255\cdot(\pi/180)$
21	$260\cdot(\pi/180)$	$10\cdot(\pi/180)$	$255\cdot(\pi/180)$	$265\cdot(\pi/180)$
22	$270\cdot(\pi/180)$	$10\cdot(\pi/180)$	$265\cdot(\pi/180)$	$275\cdot(\pi/180)$
23	$280\cdot(\pi/180)$	$10\cdot(\pi/180)$	$275\cdot(\pi/180)$	$285\cdot(\pi/180)$
24	$290\cdot(\pi/180)$	$10\cdot(\pi/180)$	$285\cdot(\pi/180)$	$295\cdot(\pi/180)$
25	$300\cdot(\pi/180)$	$10\cdot(\pi/180)$	$295\cdot(\pi/180)$	$305\cdot(\pi/180)$
26	$310\cdot(\pi/180)$	$10\cdot(\pi/180)$	$305\cdot(\pi/180)$	$315\cdot(\pi/180)$
27	$320\cdot(\pi/180)$	$10\cdot(\pi/180)$	$315\cdot(\pi/180)$	$325\cdot(\pi/180)$
28	$330\cdot(\pi/180)$	$10\cdot(\pi/180)$	$325\cdot(\pi/180)$	$335\cdot(\pi/180)$
29	$340\cdot(\pi/180)$	$10\cdot(\pi/180)$	$335\cdot(\pi/180)$	$345\cdot(\pi/180)$
30	$350\cdot(\pi/180)$	$10\cdot(\pi/180)$	$345\cdot(\pi/180)$	$355\cdot(\pi/180)$

Fig. 4 Port positions on the surface of the cylinder [1].

B. Procedure

To start the procedure, first, the room temperature and pressure are measured using a thermometer and barometer. For this experiment, the measured room temperature and pressure are **21**℃ and **750.2 mm of Hg**. Next, use the pressure scanner interface to set up the data file. The pressure scanner must be zeroed manually to remove any errors. Care must be taken to align the cylinder with the test section walls. The port 2 and 30 should read the same value of pressure if aligned properly. Next, the wind tunnel is switched on and flow is allowed to stabilize before recording the freestream dynamic pressure from the analog manometer. For this experiment, it is measured to be **40 mm of H_2O**. Then, begin data acquisition by using the computer interface to record data. After 3-5 seconds, data is collected and stored in the file [1].

IV. Results and Discussion

In this section, this report goes over the analysis and results chronologically as outlined in the lab manual. First, the lab measurements are converted to metric units for consistency.

The density is calculated using the ideal gas law with the room pressure and temperature measurements obtained for the experiment. The value for air gas constant R is taken as 287 J/(kg-K). The room pressure is converted to pascals using the conversion factor – 1 mm of Hg = 133.3224 Pa. The room temperature is converted to kelvin (K).

$$\rho_\infty = \frac{P_\infty}{RT_\infty} \tag{5}$$

The value of freestream density calculated using Eq. (5) is 1.18 kg/m^3. Using this value of freestream density and the freestream dynamic pressure measurement, the freestream velocity can be calculated by the following relation in Eq. (8) obtained from Bernoulli's equation:

$$U_\infty = \sqrt{\frac{2(P_{total} - P_\infty)}{\rho_\infty}} \tag{6}$$

Here, the difference between total pressure and freestream static pressure is the dynamic pressure. Using the Eq. (8) above, the freestream velocity obtained is $U_\infty = 25.73$ m/s. The freestream dynamic pressure is converted to pascals using the conversion factor – 1 mm of H_2O = 9.8065 Pa.

The Reynolds number is calculated by the following relationship in Eq. (7):

$$Re = \frac{\rho_\infty U_\infty D}{\mu_\infty} \tag{8}$$

The dynamic viscosity can be calculated using Sutherland's law. It gives an approximation for the viscosity of gases based on temperature, given in Eq. (9) [2].

$$\frac{\mu}{\mu_0} = \left(\frac{T}{T_0}\right)^{\frac{3}{2}} \left(\frac{T_0 + S_\mu}{T + S_\mu}\right) \tag{10}$$

Here, the term S_μ is Sutherland's constant representing the effective temperature. For air, $S_\mu = 111\ K$. The values for $T_0 = 273\ K$ and $\mu_0 = 1.716 \cdot 10^{-5}$ (N-s)/m^2 for air [2]. The room temperature was converted to a kelvin scale, $T = 294.15\ K$. Using Eq. (11), the dynamic viscosity calculated is $\mu = 1.819 \cdot 10^{-5}$ (N-s)/m^2. Using Eq. (12), the Reynolds number is 105,154.93. Since this experiment's Reynolds number $Re_D = 1.051 \cdot 10^5$, the flow lies within the subcritical regime of the range, $400 < Re_D < 3 \cdot 10^5$.

For the post-processing of the experimental data, the pressure data obtained from the pressure scanners is converted from psig to pascals using the conversion factor – 1 psig = 6894.757 Pa. For the analytical portion of the analysis, using the given pressure port positions for the experiment, the ideal surface pressure distribution was plotted using Eq. (13). Eq. (14) assumes irrotational, steady, inviscid, incompressible flow. It is obtained using Bernoulli's principle, equating the freestream properties to the properties at the edge point e on the cylinder. The two points lie on the same streamline related to Eq. (15-16) [1].

$$p_e = p_\infty + \frac{1}{2}\rho_\infty U_\infty^2 - 2\rho_\infty U_\infty^2 \sin^2\theta \tag{17}$$

$$C_p = \frac{p_e - p_\infty}{\frac{1}{2}\rho_\infty U_\infty^2} \tag{18}$$

Finally obtaining the analytical pressure coefficient relation in Eq. (19) by substituting Eq. (20) in Eq. (21).

$$C_p = 1 - 4\sin^2\theta \tag{20}$$

The port positions in i are converted to radians while using Fig. 4. The pressure coefficients obtained for the port positions in θ are plotted in Fig 6. The solid line seen in Fig. 6 is the potential flow result from Eq. (23) for the analytical part.

Moving onto the experimental portion, the pressure coefficients are obtained using the pressure scanner readings attached to the port positions of the cylinder, and the freestream dynamic pressure reading from the manometer. These are the following equations taken for obtaining the pressure coefficients in Eq. (24-27).

$$P_{total} - P_\infty = P_{pitot} = 40\ mm\ of\ H_2O \tag{21}$$

$$P_e = P_{scan} + P_{pitot} \tag{22}$$

$$P_{scan} = P_e - P_{total} \tag{23}$$

$$P_e - P_\infty = P_{scan} + P_{pitot} \tag{24}$$

Plugging Eq. (27) into Eq. (21) gives the pressure coefficient at each port location. The data file contains the port location in terms of θ_i.

For the CFD part, the mean static pressure data was extracted from the simulation results. A laminar Navier-Stokes solver is used from ANSYS Fluent to perform this analysis. The flow conditions used are two-dimensional, unsteady flow. This solver is particularly applicable only to the laminar region of the cylinder. The flow aft of the cylinder is turbulent and therefore requires turbulence models to accurately produce results. The virtual version of the cylinder is set up in the software. The cylinder is 2D, confined within a large square-shaped domain as seen in Fig. 5.

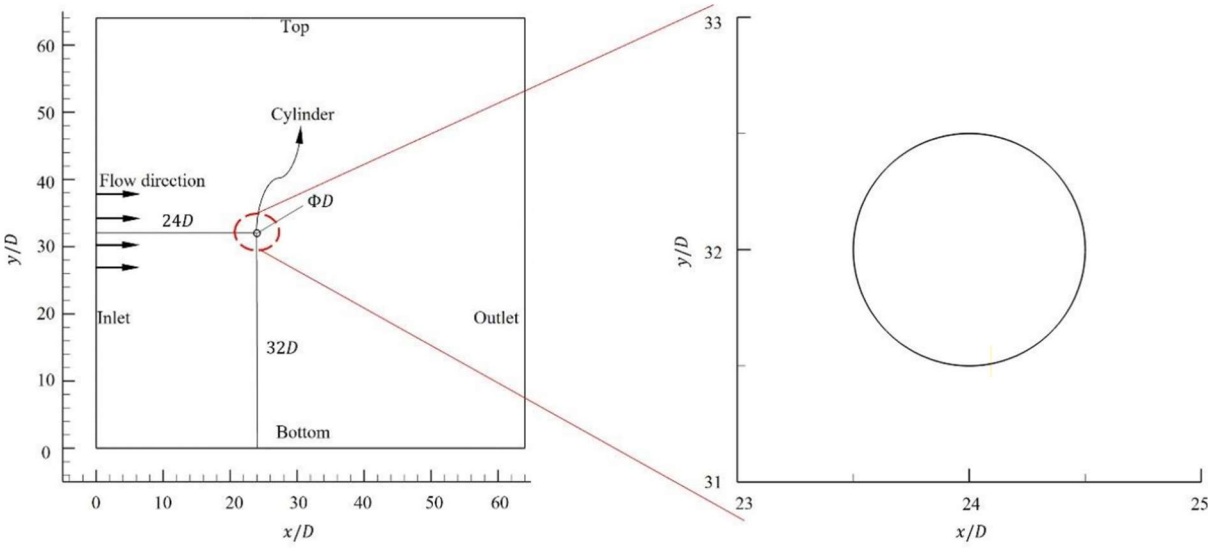

Fig. 5 Schematic of the CFD domain setup [1].

The cylinder is placed a distance $24D$ away from the inlet wall. The reference system is set up at the beginning of the inlet. The x and y axes are normalized by the cylinder diameter. This detail is important for converting the normalized values of distance to measured angles θ_i along the cylinder. The mesh used is a monotonic rational quadratic spline (MRDS) distribution. It has finer grids closer to the surface of the cylinder to improve accuracy. Due to computational time and energy constraints, the meshes away from the cylinder are kept larger [1].

As for the boundary conditions of the domain, the inlet specified is selected to be a velocity inlet with a freestream velocity of 25 m/s. The boundary at which the incoming flow is specified is selected as the inlet whereas, the other three boundaries are the outlets. A no-slip condition is chosen to keep the velocity at the wall zero [1]. Using the CFD video and case file provided, the simulation is set, and mean static pressure data and wall shear stress data are extracted.

The locations of x_i are not given in the data file. The normalized locations must be used to convert the distances to measured angles θ_i using the following:

$$x_i = D\left(\frac{\left(\frac{x}{D}\right)_i - 1.4805}{1.5435 - 1.4805}\right) \tag{25}$$

The x-location obtained from the CFD results is a non-dimensional value of x/D. Since the cylinder is placed at a distance of $24D$ from the inlet wall, the location must converted such that the leading edge of the cylinder is the starting point. For this, the starting and ending locations of the cylinder were obtained in terms of x/D at 1.4805 and 1.5435, respectively. The values were used to normalize and find the x-location data on the cylinder using Eq. 29.

Then, the angle θ_i can be obtained using the following transformation:

$$\cos\theta_i = \frac{(R - x_i)}{R} \tag{26}$$

Here, θ_i corresponds to the angular location of x_i extracted from the CFD data. The same relation was used for finding the measured angle corresponding to wall shear stress distribution from CFD results. Once the measured angle locations are obtained, care must be taken to segregate the upper and lower surface data using filters. There are two data points for the same x_i location, each for the upper and lower surfaces. Data must be arranged in ascending order and segregated for upper and lower surfaces. The angular measure θ_i is subtracted from 2π to obtain locations for the lower surface.

The pressure coefficients are calculated using the same method as experimental for CFD. The pressure profiles for the ideal inviscid case, experimental, and CFD results are plotted together in Fig. 6.

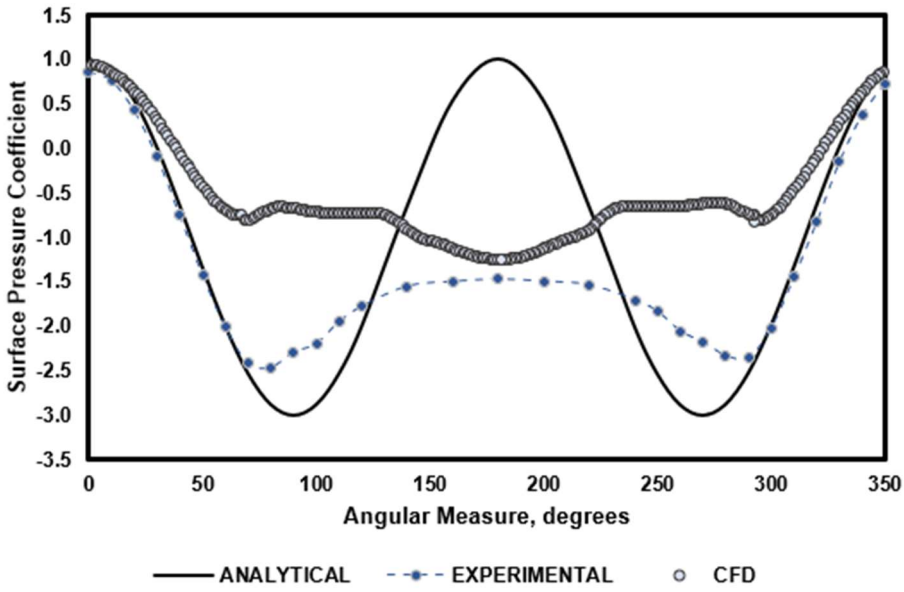

Fig. 6 Superimposing analytical, experimental, and CFD pressure coefficient results.

From Fig. 6, for the ideal pressure profile (the solid line) from the inviscid potential flow predictions, the flow separation does not occur since there are no viscous phenomena. For the experimental results, the flow separation region is approximated to be the region where the pressure profile begins to plateau. In Fig. 6, the results show that at approximately $\theta = 120°$, the pressure profile begins to flatten, hence, it can be regarded as the separation location. For the CFD results, the separation location appears to be much earlier at around $\theta = 80.4°$.

With the approximate location of flow separation for all three methods, the drag coefficients can be calculated. For the experimental results, the wall static pressure p_i at each port position is needed. The experimental drag force F_D is obtained using length L, radius R of the cylinder and, starting $\theta_{i,s}$ and final $\theta_{i,f}$ port positions are given in Fig. (4). The experimental drag force can then be calculated in a discretized manner using Eq. (30).

$$F_{D,exp} \approx \sum_{i=1}^{30} p_i \cdot L \cdot R \cdot (\sin\theta_{i,f} - \sin\theta_{i,s}) \tag{27}$$

The port position angles are kept in radians. From the relation above, the drag coefficient is obtained by using Eq. (31).

$$C_{D,exp} = \frac{F_{D,exp}}{\frac{1}{2}\rho_\infty U_\infty^2 A_{ref}} \tag{28}$$

Due to the effects of wall confinement, the force and moments on the cylinder surface may alter the results obtained. Thus, to account for this limitation, the equation provided by Allen and Vincenti is used, as seen in Eq. (32). This provides a corrected drag coefficient for the experimental data. The corrected drag coefficient is obtained for the top and bottom surfaces of the cylinder. Additionally, the total corrected drag coefficient is also presented in Table 1.

$$\frac{C_{Dc}}{C_D} = 1 - \frac{1}{2} C_D \left(\frac{D}{H}\right) - 2.5 \left(\frac{D}{H}\right)^2 \tag{29}$$

The symbol H in Eq. (32) represents the height of the wind tunnel test section, which is 12" for this experiment. Also, D is the characteristic length of the cylinder (diameter) [1].

Table 1. Experimental data drag and drag coefficient results.

	C_D	Drag, D [N]	Corrected C_D
Upper surface	0.8039	6.0015	0.6493
Lower surface	0.3595	2.6842	0.3071
Total	1.1634	8.6857	0.9564

Using the surface pressure data from CFD results, the pressure drag and drag coefficient are calculated to compare with experimental values. Since the CFD simulation is 2D, the length of the cylinder is taken as 1. The frontal reference area of the cylinder is taken as the area of a circle, πr^2. The radius of the cylinder remains the same. The default value for density used is $\rho = 1.225$ kg/m^3 from the simulation setup. Using the slightly different values, and Eq. (30-31), the drag coefficient calculated is 0.5423 with a pressure drag value of 0.674 N.

Lastly, an accurate curve fit from Sucker and Brauer is used to obtain the drag coefficient for the analytical method. This Eq. (33) applies to the Reynolds number range of $10^{-4} < Re_D < 250{,}000$ [1].

$$C_D \approx 1.18 + \frac{6.8}{Re_D^{0.89}} + \frac{1.96}{Re_D^{0.5}} - \frac{0.0004 Re_D}{1 + (3.64 \cdot 10^{-7}) Re_D^2} \tag{30}$$

The results from all four methods of calculating drag coefficients are tabulated in Table 2 below.

Table 2. Experimental data drag and drag coefficient results.

Methods	C_D
Experimental Results	1.1634
Wall confinement correction	0.9564
CFD Results	0.5423
Sucker and Brauer Fit	1.1758

As seen from the results in Table 2 above, the drag coefficient from experimental results is close to drag coefficient obtained from the literature fit data by Sucker and Brauer. The CFD drag coefficient is much lower than the other three methods. This could be due to the nature of the simulation that was set up. As seen in Fig. 6, the pressure distribution for CFD results is less drastic, with a smaller range of pressure coefficient from 1.0 to -1.5. The reason for this inconsistency could be due to the need for a finer mesh size during simulation or higher accuracy turbulence models. For the CFD simulation, a laminar viscous model was used. Additionally, the fluid properties used for the simulation were different from the experimentally measured data, specifically, with values of air density and viscosity.

To obtain a more specific point of flow separation, the experimental results are examined as given in Table. 3.

Table 3. Experimental data of coefficient of pressure.

Port Position, θ_i [°]	C_p
0.00	0.860213568

10.00	0.764657920
20.00	0.430362557
30.00	-0.085631614
40.00	-0.744491709
50.00	-1.415130158
60.00	-2.006065662
70.00	-2.418578712
80.00	-2.469604767
90.00	-2.298058439
100.00	-2.201045657
110.00	-1.957004716
120.00	**-1.781289122**
140.00	-1.551963652
160.00	-1.499777514
180.00	-1.471237726
200.00	-1.496629472
220.00	-1.535901782
240.00	-1.705280865
250.00	-1.834804081
260.00	-2.055469359
270.00	-2.182197831
280.00	-2.331992611
290.00	-2.357231437
300.00	-2.019028705
310.00	-1.449869357
320.00	-0.826374203
330.00	-0.146117615
340.00	0.382201554
350.00	0.734392070

Upon examining the experimental data and results in Table 3, the coefficient of pressure C_p starts to stagnate and also maintain from $\theta = 120°$ with $C_p = -1.78$. This is the separation point for experimental data.

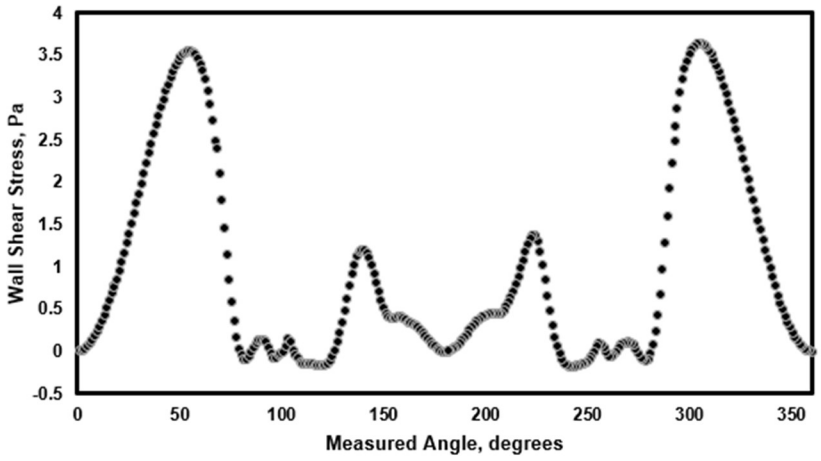

Fig. 7 Wall shear stress distribution over the cylinder.

Now, using the CFD wall shear stress data in the x-direction, the skin friction distribution can be obtained using Eq. 34. The wall shear stress and skin friction coefficient against the measured angle are plotted in Fig. 7-8.

$$C_f = \frac{\tau_{wx}}{\frac{1}{2}\rho_\infty U_\infty^2} \tag{31}$$

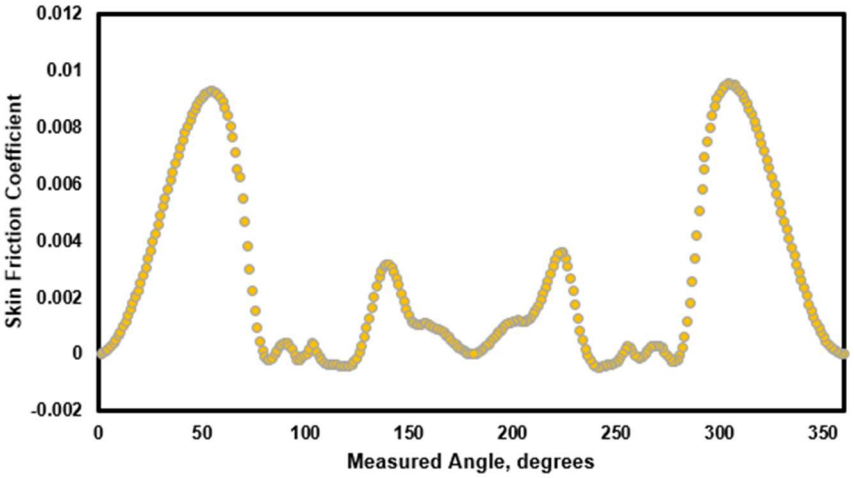

Fig. 8 Skin friction coefficient profile on the cylinder.

The value of the skin friction coefficient when it first goes to zero is the separation point on the cylinder. Using the CFD results obtained, the location at which $C_f = 0.0000974$ is at $\theta = 79.2°$. The location in terms of θ is obtained from the same method as for the CFD pressure profile.

For the analytical calculation of the boundary layer separation point, the Thwaites-Walz method is performed on the inviscid-ideal velocity profile and corrected velocity profile using Hiemenz flow on the top surface. This method uses a momentum thickness relationship to give an approximate location of separation. When $\Lambda(x_{sep}) \approx -0.09$ is the location of the separation point. The momentum thickness is given by Eq. (35):

$$\Lambda(x) = \frac{0.45}{U_e(x)^6}\left(\int_0^x U_e^5(x)\ dx\right)\left(\frac{dU_e(x)}{dx}\right) \tag{32}$$

The edge velocity U_e is determined using the following two methods and compared: inviscid ideal velocity profile in Eq. (36) and Hiemenz flow in Eq. (37). The Eq. (37) is applicable for a subcritical regime of $Re_D \sim 10^4$ [1].

$$\frac{U_e(x)}{U_\infty} = 2\sin\left(\frac{x}{R}\right) = 2.0\left(\frac{x}{R}\right) - 0.333\left(\frac{x}{R}\right)^3 + 0.0167\left(\frac{x}{R}\right)^5 \tag{33}$$

$$\frac{U_e(x)}{U_\infty} = 1.814\left(\frac{x}{R}\right) - 0.271\left(\frac{x}{R}\right)^3 - 0.0471\left(\frac{x}{R}\right)^5 \tag{34}$$

The following are the results for the Thwaites-Walz method in Table 4-5.

Table 4. Thwaites-Walz method results for Hiemenz flow velocity profile.

Port Number	θ_i [°]	U_e [m/s]	x_i [m]	$\Lambda(x)$
1	0	0.00	0.0000	0.0000
2	10	8.11	0.0055	6.7371
3	20	15.99	0.0110	0.8017
4	30	23.39	0.0165	0.2852

5	40	30.01	0.0220	0.1358
6	50	35.49	0.0275	0.0655
7	60	39.35	0.0330	0.0212
8	70	41.01	0.0385	-0.0127
9	80	39.76	0.0440	-0.0431
10	**90**	**34.70**	**0.0495**	**-0.0764**
11	100	24.77	0.0550	-0.1471
12	110	8.66	0.0605	9.5130
13	120	-15.14	0.0660	10267.4718
14	140	-93.25	0.0770	28.1921
15	160	-227.33	0.0880	5.9722
16	180	-440.48	0.0990	-0.2250

Table 5. Thwaites-Walz method results for inviscid flow velocity profile.

Port Number	θ_i [°]	U_e [m/s]	x_i [m]	$\Lambda(x)$
1	0	0.00	0.0000	0.0000
2	10	8.94	0.0055	6.6850
3	20	17.60	0.0110	0.7979
4	30	25.73	0.0165	0.2899
5	40	33.08	0.0220	0.1469
6	50	39.42	0.0275	0.0836
7	60	44.57	0.0330	0.0479
8	70	48.36	0.0385	0.0245
9	80	50.68	0.0440	0.0072
10	90	51.47	0.0495	-0.0066
11	100	50.68	0.0550	-0.0185
12	110	48.36	0.0605	-0.0294
13	**120**	**44.57**	**0.0660**	**-0.0711**
14	140	33.08	0.0770	-0.1098
15	160	17.60	0.0880	-0.2250
16	180	0.00	0.0990	-0.2250

From Tables 4-5, the separation location for the inviscid flow velocity profile occurs at $\theta = 120°$ and the Hiemenz method is at $\theta = 90°$, approximately. Note, that the data is given for only the top surface.

Upon examining the separation points for analytical, experimental, and CFD results, there are some key differences. The analytical inviscid flow velocity profile method and experimental data separation points are the same at $\theta = 120°$. The CFD results and Hiemenz flow method results are close at $\theta = 79.2°$ and $\theta = 90°$.

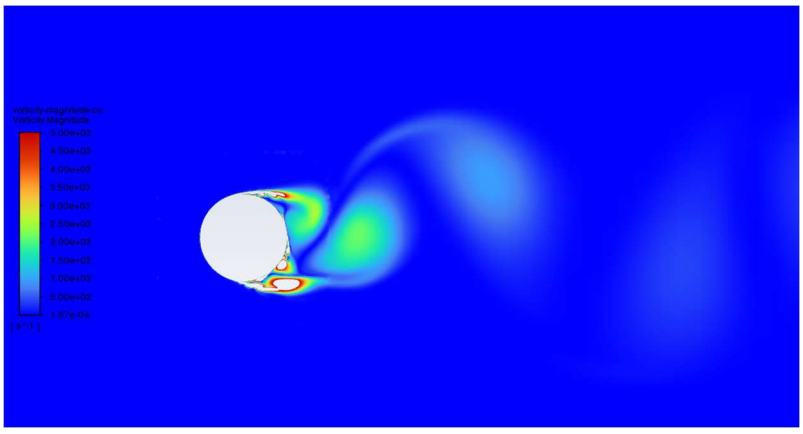

Fig. 9 Vortex shedding and the contours of vorticity magnitude.

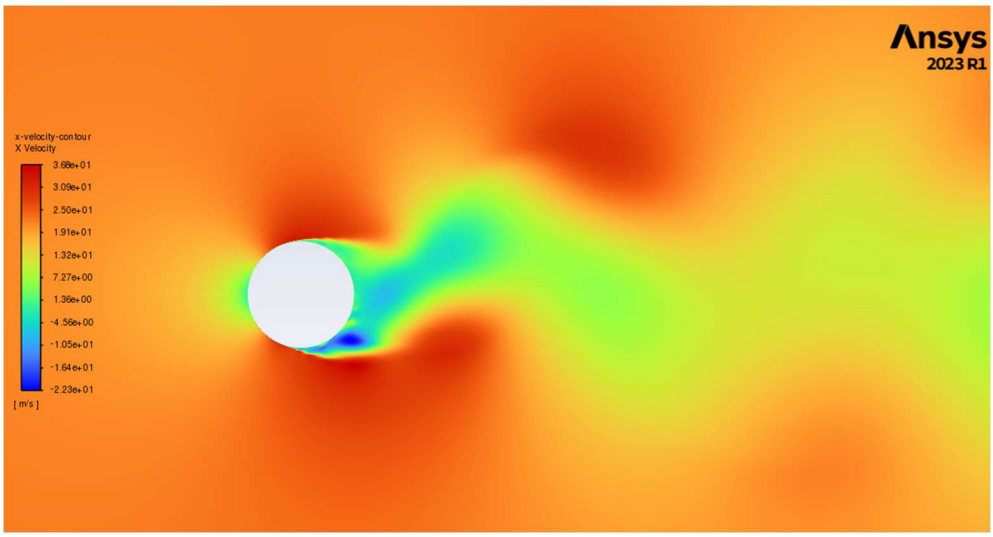

Fig. 10 Velocity contour CFD plot using ANSYS Fluent.

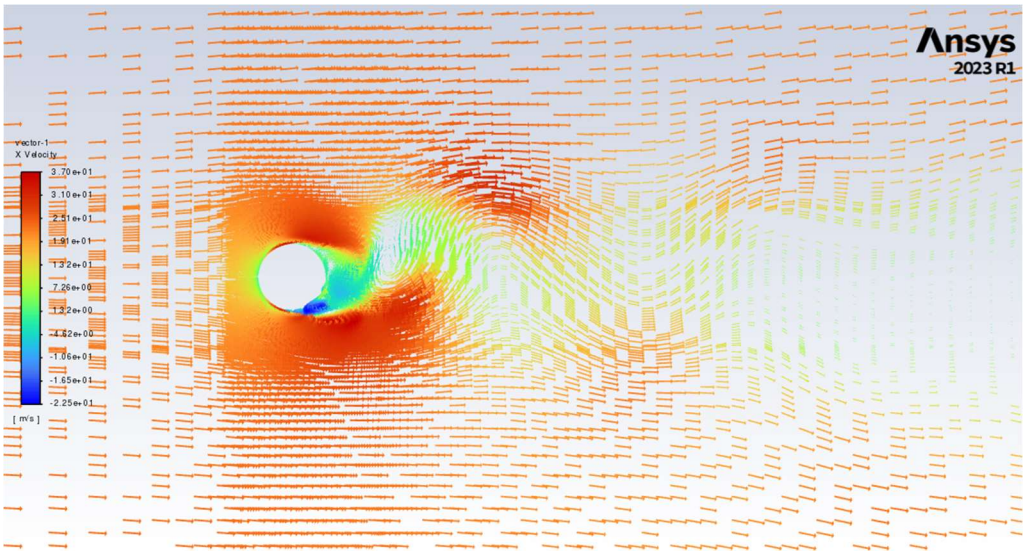

Fig. 11 Velocity vectors colored x-velocity plot using ANSYS Fluent.

The following in Fig. 9-11 shows the simulation results for contours of vorticity magnitude and vortex shedding on the aft portion of the cylinder. As seen, there is a large wake region behind the cylinder that is turbulent.

With a real flow analysis, the boundary layer thickness δ is added such that $r = R + \delta$. Where R is the radius of the cylinder. The position vector r points to a point on the streamline passing through the boundary layer. This is the case where the difference in pressure at the point e on the streamline and surface of the cylinder is large and normal to the wall. If there is no significant difference, such as in the case of ideal, inviscid flow – then the boundary layer edge pressure and wall pressure are approximately the same $p_e \approx p_w$. Then, Bernoulli's principle can be used to find the edge velocity where the streamline passes right along the surface of the cylinder. Additionally, this assumption becomes invalid if the boundary layer thickness is too large when compared to the radius of the cylinder [1].

The experimental data is used to plot the edge velocity profile over a cylinder using Bernoulli's principle given in Eq. (38) and Fig. 12. This equation is only applicable until the point of flow separation where $x = x_{sep}$.

$$U_e = \sqrt{\frac{2}{\rho_\infty}\left(p_{o,\infty} - p_w\right)} \qquad p_{o,\infty} = p_\infty + \frac{1}{2}\rho_\infty U_\infty^2 \tag{35}$$

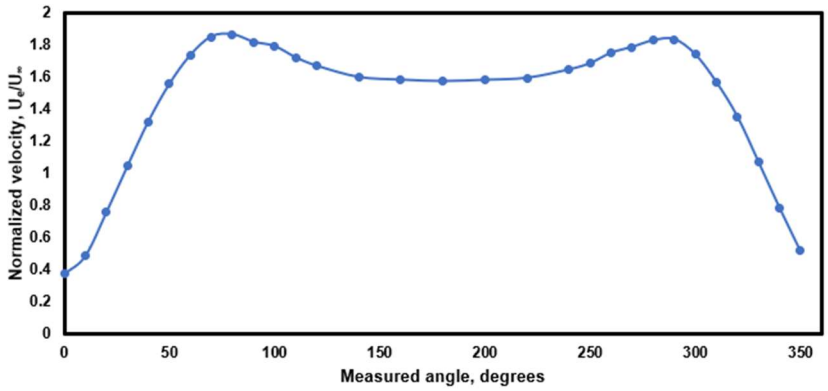

Fig. 12 The edge velocity profile over the cylinder using Bernoulli's principle.

Ideal edge velocity is given by the following in Eq. (39) from potential flow analysis. Viscous effects are neglected.

$$U_e = v_{\theta \ at \ r=R} = 2U_\infty \sin\theta \qquad v_{r \ \ at \ \ r=R} = 0 \tag{36}$$

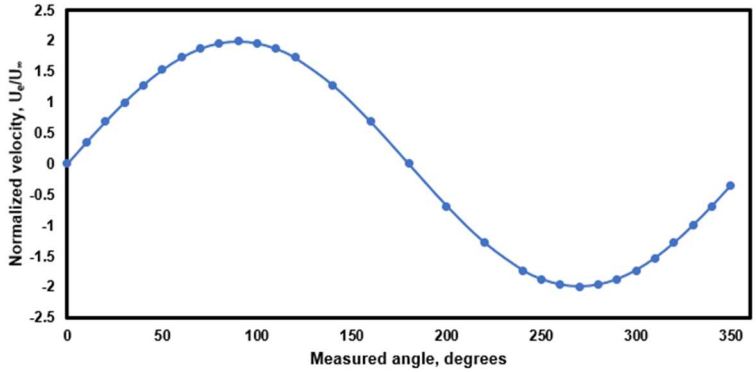

Fig. 13 Edge velocity profile over cylinder using ideal potential flow.

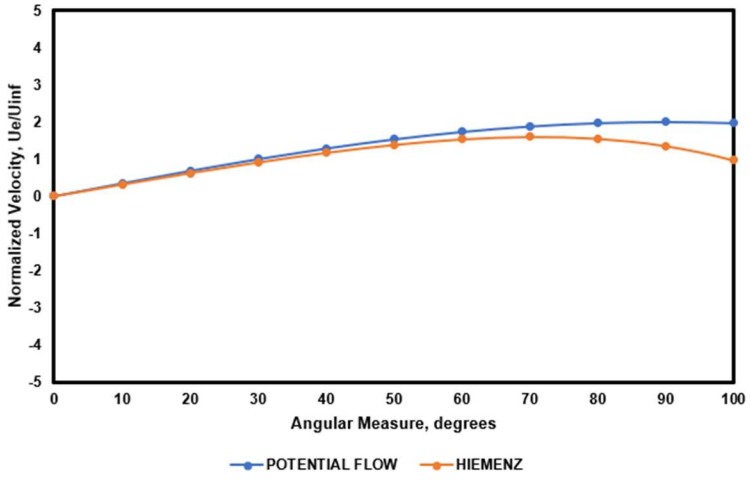

Fig. 14 Potential flow and Hiemenz edge velocity profiles.

When compared to the velocity distribution of Hiemenz, the inviscid case follows a similar trend before deviating at $\theta = 30°$. The normalized velocity peaks at $\theta = 70°$ after which it completely deviates from the inviscid velocity profile. The inviscid velocity profile has a peak at $\theta = 100°$, following a sinusoidal trend.

The reduced order boundary layer analysis cannot be directly used for flow over bluff bodies. Due to the strong coupling of the viscous and inviscid phenomena at the aft region of the cylinder, the disturbances propagate upstream, to the forebody region. This strong coupling alters the pressure and velocity distribution during separation.

(EXTRA CREDIT)

The Reynolds number for the new freestream velocity of $U_\infty = 10$ m/s is 43128.98. The value of freestream density is taken as $\rho_\infty = 1.225$ kg/m^3, the same value used in the CFD simulation. The value of dynamic viscosity used is, $\mu_\infty = 0.000017894$ (N-s)/m^2. These are default values from the CFD simulation.

The length of the domain is taken to be 64 times the diameter of the cylinder ($64 \cdot D$), equal to 4.032 m. With the new free stream velocity, the flow through time can be determined using Eq. (40):

$$t_f = \frac{64 \cdot D}{U_\infty} = 0.4032 \text{ seconds} \tag{37}$$

The Strahaul number can be calculated using Eq. (41) below.

$$St = \frac{fD}{U_\infty} \approx 0.2 \tag{38}$$

Using Eq. (41), the calculated frequency f is 31.75 Hz. Then, the sampling frequency is taken to be 25 times the frequency. The Nyquist criterion states that the sampling frequency must be at least twice the frequency. The corresponding time scale is the inverse of the sampling frequency [3].

$$t = \frac{1}{25f} = 1.26 \cdot 10^{-3} \text{ seconds} \tag{39}$$

The number of time steps needed are obtained using Eq. (43).

$$n = \frac{5t_f}{t} = 1600.2 \tag{40}$$

Using Fig. 15, the location of flow separation appears to occur around $\theta \approx 80°$, specifically beginning from $\theta = 84.00°$, where the pressure coefficient C_p maintains at -2.55.

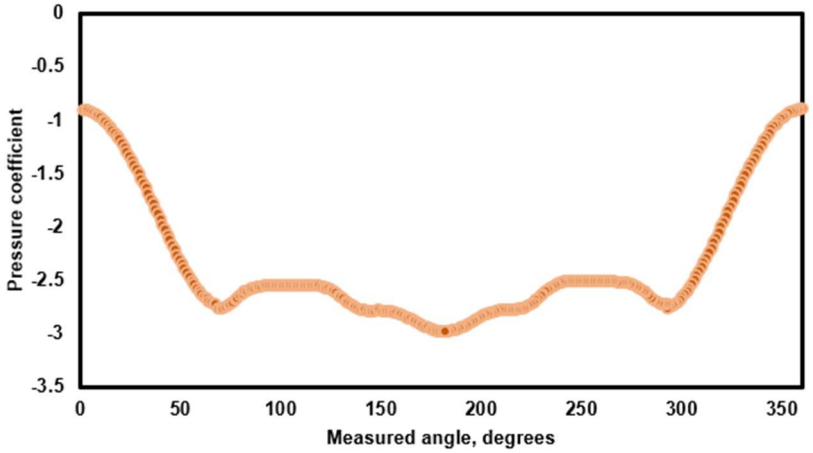

Fig. 15 Pressure coefficient over the cylinder for CFD extra credit results.

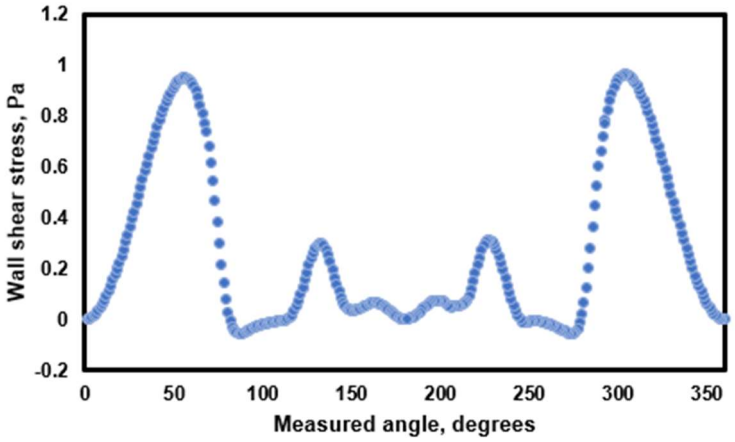

Fig. 16 Wall shear stress over the cylinder for CFD extra credit results.

The separation point for the new CFD simulation using wall shear stress data occurs when the shear stress is 0.030094. This point is at $\theta_i = 80.4°$. It is the first value of shear stress and skin friction coefficient when close to zero, as noted earlier.

V. Conclusion

In this experiment, a 2D circular cylinder is used to analyze the flow over a bluff body. Specifically, the flow over the cylinder in the subcritical regime is studied using experimental data and CFD simulation. Various analytical, numerical, and experimental methods are employed to understand the edge velocity distribution, drag coefficient calculation, the pressure distribution over the surface and by determining the separation location. The Reynolds number of the experiment lies within the subcritical regime at $Re_D = 1.051 \cdot 10^5$. The pressure coefficients for the analytical, CFD, and experimental are plotted together at the flow separation locations and are estimated. For CFD, the flow separates at $\theta = 80.4°$, and for experimental data it is at $\theta = 120°$. The deviation from the ideal and CFD results could be due to the roughness of the cylinder.

Then, the drag coefficient is computed for four different approaches – experimental, wall confinement corrected, CFD results, and literature fit data. The drag coefficients for experimental and literature fit data are very close at 1.16 and 1.17, respectively. However, the drag coefficient for the CFD result was much lower at 0.54. This could be due to the laminar model used during simulation. Additionally, the default parameters used for CFD simulation may give slightly different results. The pressure coefficient data was examined to determine the location of flow separation, occurring at $\theta = 120°$. Using the CFD results to obtain the skin friction coefficient, the flow separation point occurs at $\theta = 79.2°$. Using the Thwaites-Walz method, the separation point was determined to be at $\theta = 120°$ for the ideal, inviscid case and at $\theta = 90°$ for the Hiemenz method.

The edge velocity profile was estimated using Bernoulli's principle, potential flow theory, and Hiemenz method. The highest edge velocity occurred at $\theta_i = 70°$ for the Hiemenz method and $\theta_i = 100°$ for the ideal, inviscid method. Bernoulli's principal method yielded the highest normalized velocity at $\theta_i \approx 80°$.

Using the case file provided, the CFD simulation was rerun for different a velocity of 10 m/s where the new Reynolds number was 43128.98. The pressure coefficient distribution yielded a separation location of $\theta = 84.00°$. The time step size was calculated using the Strahaul number giving $1.26 \cdot 10^{-3}$ seconds. Upon examining the wall shear stress data, the separation point was noted at $\theta_i = 80.4°$.

References

[1] "MAE 3182 Flow Over a Cylinder Lab Manual Fall 2023," The University of Texas at Arlington, MAE Department.

[2] “Sutherland’s Law.” Retrieved 31 October 2023. https://doc.comsol.com/5.5/doc/com.comsol.help.cfd/cfd_ug_fluidflow_high_mach.08.27.html
[3] “The Flow Over a Cylinder CFD Simulation Tutorial.”